

Comparison of the performance of high-order schemes based on the gas-kinetic and HLLC fluxes

Xiaojian Yang^a, Xing Ji^b, Wei Shyy^a, Kun Xu^{a,b,c,*}

^a*Department of Mechanical and Aerospace Engineering, Hong Kong University of Science and Technology, Clear Water Bay, Kowloon, Hong Kong*

^b*Department of Mathematics, Hong Kong University of Science and Technology, Clear Water Bay, Kowloon, Hong Kong*

^c*Shenzhen Research Institute, Hong Kong University of Science and Technology, Shenzhen, China*

Abstract

In this paper, a comparison of the performance of two high-order finite volume methods based on the gas-kinetic scheme (GKS) and HLLC fluxes is carried out in structured rectangular mesh. For both schemes, the fifth-order WENO-AO reconstruction is adopted to achieve a high-order spatial accuracy. In terms of temporal discretization, a two-stage fourth-order (S2O4) time marching strategy is adopted for WENO5-AO-GKS scheme, and the fourth-order Runge-Kutta (RK4) method is employed for WENO5-AO-HLLC scheme. For the viscous flow computation, the GKS includes both inviscid and viscous fluxes in the evolution of a single cell interface gas distribution function. While for the WENO5-AO-HLLC scheme, the inviscid flux is provided by HLLC Riemann solver, and the viscous flux is discretized by a sixth-order central difference method. Based on the tests of forward Mach step and viscous shock tube, both schemes show outstanding shock capturing property. From the Titarev-Toro and double shear layer tests, WENO5-AO-GKS scheme seems to have a better resolution than WENO5-AO-HLLC scheme. Both schemes show excellent robustness in extreme cases, such as the Le Blanc problem. From the cases of the Noh problem and the compressible isotropic turbulence, WENO5-AO-GKS scheme shows favorite robustness. In the compressible isotropic turbulence and three-dimensional Taylor-Green vortex problems, WENO-AO-GKS can use a CFL number up to 0.5, instead of 0.3 for WENO5-AO-HLLC. In terms of computational efficiency, WENO5-AO-HLLC scheme is about 27% more expensive than WENO5-AO-GKS scheme in the two-dimensional viscous flow problems, but is about 15% faster in the three-dimensional case, because WENO5-AO-GKS scheme needs multidimensional spatial reconstruction for flow variables in both one normal and two tangential directions in the 3D case. Due to the multi-dimensionality, WENO5-AO-GKS scheme performs better than WENO5-AO-HLLC scheme in the laminar boundary layer and the double shear layer test.

Keywords: WENO-AO reconstruction, gas-kinetic scheme (GKS), HLLC Riemann solver.

*Corresponding author

Email addresses: xyangbm@connect.ust.hk (Xiaojian Yang), xjiad@connect.ust.hk (Xing Ji),

1. Introduction

The development of high-order schemes has been the main research direction in the current computational fluid dynamics. The targeting scheme should be accurate, robust, and efficient. The finite volume scheme is mainly composed of spatial reconstruction, flux evaluation, and temporal discretization. The successful high-order reconstructions include the essentially non-oscillatory (ENO) and weighted essentially non-oscillatory (WENO) scheme [13, 18, 23]. There exists many modified versions of WENO, such as WENO-JS [18], WENO-Z [4], central WENO (CWENO) [19], WENO with adaptive order (WENO-AO) [1], multi-resolution WENO [45], etc.

Besides the importance of initial reconstruction, the flux evaluation and temporal updating method also play important roles in the determination of the quality of the schemes. In the past decades, the gas-kinetic scheme (GKS) is mainly focusing on the time accurate flux function for capturing the Euler and Navier-Stokes solutions. The GKS is based on the kinetic Bhatnagar-Gross-Krook (BGK) model and the Chapman-Enskog expansion is used for the flux evaluation [3, 8]. The scheme has been systematically developed for the flow computation from low-speed to hypersonic one [39, 40]. In GKS, a time-dependent gas distribution function at the cell interface is obtained and covers a physical process from the kinetic free particle transport to the hydrodynamic NS wave propagation. In the smooth region, GKS can accurately recover the Euler or Navier-Stokes solution. In the discontinuity region, the particle free transport mechanism introduces the numerical dissipation within a shock layer and stabilize the numerical shock structure. Different from the traditional CFD methods based on the macroscopic governing equations directly, GKS has multi-scale property. Depending on the ratio of time step Δt over the particle collision time τ , the flux function in GKS makes a smooth transition from the upwind flux vector splitting (kinetic scale) to the central difference (hydrodynamic scale). GKS has been adopted in multicomponent flow [38, 26], acoustic computation [43], turbulence simulation [22, 7, 30], and hypersonic flow [21], etc. Furthermore, a unified GKS (UGKS) has been developed for all flow regimes from rarefied to continuum one [41]. At the same time, in order to develop high-order GKS, many techniques in CFD have been used in the kinetic schemes. The WENO reconstruction has been adopted to improve spatial accuracy [24]. Also, the high-order compact GKS on both structured and unstructured meshes have been developed [14, 17, 44]. Since the flux function in GKS is time-dependent, which provides not only the numerical flux but also its time derivative. Therefore, multi-stage multi-derivative (MSMD) methods can be employed for time marching in GKS [16]. Particularly, a two-stage fourth-order (S2O4) temporal discretization for GKS has been developed with favorable numerical performance [28, 27].

In the CFD community, mostly the exact or approximate Riemann problems are used in the flux construction [11]. One of the outstanding approximate Riemann solvers is the HLL flux [12]. In HLL, a configuration including two waves and three constant states is assumed. In order to improve the capacity of capturing contact surfaces in HLL solver, Toro

presented a modified version of HLL-type Riemann solver, which was called Harten-Lax-van Leer contact (HLLC), to resolve the contact discontinuity in wave structure and show better resolution of intermediate waves [36]. In HLLC solver, the priori estimate of the fastest and slowest wave emerging from the initial discontinuity is needed, and several methods have been proposed [34]. Since the HLLC flux is time-independent, the Runge-Kutta (RK) method is usually employed for updating the solution in time. HLLC Riemann solver has been successfully used in the simulation of two-phase flow [33], combustion [9], turbulence [2], etc. More details and extensions of the HLLC Riemann solver be found in the review paper under the finite volume and discontinuous Galerkin frameworks [35].

There are differences between GKS and Riemann solver based schemes. In GKS, the inviscid and viscous terms are coupled together in the flux evaluation from a time-dependent gas distribution function, where the spatial derivatives in the normal and tangential directions are included in the time evolution of the gas distribution function. The current study is to make a comparison of the performance in inviscid and viscous flow simulations between GKS and HLLC Riemann solver in terms of accuracy, robustness, efficiency, and stability. The same fifth-order WENO-AO reconstruction is employed to minimize the differences in spatial discretization for these two schemes. In WENO-AO reconstruction, both the point-wise quantities and the corresponding spatial derivatives are provided as the initial state [15]. Besides, S2O4 temporal discretization is used for GKS, and fourth-order Runge-Kutta (RK4) is adopted for HLLC solver, while both time marching schemes achieve the same temporal accuracy. For convenience, the above two schemes are named as WENO5-AO-GKS and WENO5-AO-HLLC schemes.

This paper is organized as follows. In Section 2, the WENO-AO reconstruction, GKS, and HLLC Riemann solver are introduced. Section 3 presents the simulation results of many test cases by WENO5-AO-GKS and WENO5-AO-HLLC schemes. Section 4 provides the computational efficiency of these two schemes. The last section is the conclusion.

2. WENO-AO-GKS and WENO-AO-HLLC

2.1. WENO-AO reconstruction

The WENO-AO reconstruction was proposed by Balsara et al. [1]. To meet the requirement for a fourth-order scheme in both space and time, the fifth-order WENO5-AO reconstruction is selected. Assume that \bar{Q} is the cell-averaged variable, and Q is the reconstructed variable. Both \bar{Q} and Q can be conservative or characteristic variables. To achieve fifth-order spatial accuracy for Q , three sub-stencils S_k , $k = 0, 1, 2$ are used to reconstruct the left $Q_{i+1/2}^l$ and right $Q_{i-1/2}^r$ interface values at $x_{i-1/2}$ and $x_{i+1/2}$. These three sub-stencils S_k are,

$$S_0 = \{I_{i-2}, I_{i-1}, I_i\}, \quad S_1 = \{I_{i-1}, I_i, I_{i+1}\}, \quad S_2 = \{I_i, I_{i+1}, I_{i+2}\}.$$

For each sub-stencil S_k , a unique quadratic polynomial $p_k^{r3}(x)$ is constructed by the requirements,

$$\frac{1}{\Delta x} \int_{I_{i-j-k-1}} p_k^{r3}(x) dx = \bar{Q}_{i-j-k-1}, \quad j = -1, 0, 1, \quad (1)$$

and each $p_k^{r3}(x)$ achieves a third-order spatial accuracy in smooth flow region.

On a large stencil $\mathbb{S}_3 = \{S_0, S_1, S_2\}$, a unique fourth-order polynomial $p_3^{r5}(x)$ is obtained by

$$\frac{1}{\Delta x} \int_{I_{i+j}} p_3^{r5}(x) dx = \bar{Q}_{i+j}, \quad j = -2, -1, 0, 1, 2.$$

After determining the above reconstructions based on different stencils, $p_3^{r5}(x)$ is defined again as,

$$p_3^{r5}(x) = \gamma_3 \left[\frac{1}{\gamma_3} p_3^{r5}(x) - \sum_0^2 \frac{\gamma_k}{\gamma_3} p_k^{r3}(x) \right] + \sum_0^2 \gamma_k p_k^{r3}(x), \quad (2)$$

where γ_k , $k = 0, 1, 2, 3$ are linear weights. According to Balsara et al. [1], the coefficients are given by

$$\gamma_3 = \gamma_{Hi}, \quad \gamma_0 = \gamma_2 = (1 - \gamma_{Hi})(1 - \gamma_{Lo})/2, \quad \gamma_1 = (1 - \gamma_{Hi})\gamma_{Lo},$$

where $\gamma_{Hi} \in [0.85, 0.95]$ and $\gamma_{Lo} \in [0.85, 0.95]$. Obviously, the above formulas satisfy $\sum_0^3 \gamma_k = 1$ and $\gamma_k > 0$, $k = 0, 1, 2, 3$. In the current study, $\gamma_{Hi} = 0.85$ and $\gamma_{Lo} = 0.85$ are used.

To deal with discontinuities, the WENO-Z type [4] non-linear weights are adopted,

$$\omega_k = \gamma_k \left[1 + \frac{\delta^2}{(\beta_k + \epsilon)^2} \right],$$

where δ is the global smooth indicator, and it is defined as

$$\delta = \frac{1}{3} (|\beta_3^{r5} - \beta_0^{r3}| + |\beta_3^{r5} - \beta_1^{r3}| + |\beta_3^{r5} - \beta_2^{r3}|) = O(\Delta h^4).$$

More specifically, $\beta_k = \beta_k^{r3}$, $k = 0, 1, 2$, are the smooth indicator of sub-stencil S_k , and $\beta_3 = \beta_3^{r5}$ is the smooth indicator of the large stencil \mathbb{S}_3 . The explicit formulas of β_k can refer to [1]. Besides, ϵ is a positive small number to avoid zero for denominator with $\epsilon = 10^{-8}$. Then, the normalized weights $\bar{\omega}_k$ can be defined as follows,

$$\bar{\omega}_k = \frac{\omega_k}{\sum_0^3 \omega_q}.$$

The final form of the reconstructed polynomial can be written as,

$$P^{AO(5,3)}(x) = \bar{\omega}_3 \left[\frac{1}{\gamma_3} p_3^{r5}(x) - \sum_0^2 \frac{\gamma_k}{\gamma_3} p_k^{r3}(x) \right] + \sum_0^2 \bar{\omega}_k p_k^{r3}(x). \quad (3)$$

The reconstructed left interface value $Q_{i+1/2}^l$ and the corresponding derivative become,

$$Q_{i+1/2}^l = P^{AO(5,3)}(x_{i+1/2}), \quad (Q_x^l)_{i+1/2} = P_x^{AO(5,3)}(x_{i+1/2}).$$

Similarly, the right interface value $Q_{i-1/2}^r$ and its derivative can also be determined by,

$$Q_{i-1/2}^r = P^{AO(5,3)}(x_{i-1/2}), \quad (Q_x^r)_{i-1/2} = P_x^{AO(5,3)}(x_{i-1/2}).$$

The reconstructed value and its normal derivative at the Gaussian quadrature points are obtained from the above procedure. Since GKS needs not only normal derivatives (Q_x), but also tangential derivative (Q_y, Q_z), the multi-dimensional reconstruction is performed. The details are given in [15].

2.2. WENO5-AO-GKS scheme

2.2.1. BGK equation and gas-kinetic scheme

Here the GKS in 2D case is presented and the scheme in 3D can be obtained similarly. The two-dimensional BGK equation is written as [3],

$$f_t + \mathbf{u} \cdot \nabla f = \frac{g - f}{\tau}, \quad (4)$$

where \mathbf{u} is the particle velocity, f is the gas distribution function, g is the corresponding equilibrium state, and τ is the collision time. The collision term satisfies the compatibility condition

$$\int \frac{g - f}{\tau} \boldsymbol{\psi} d\Xi = 0, \quad (5)$$

where $\boldsymbol{\psi} = (1, u, v, \frac{1}{2}(u^2 + v^2 + \xi^2))^T$, the internal variables $\xi^2 = \xi_1^2 + \dots + \xi_K^2$, $d\Xi = dudvd\xi_1 \dots d\xi_K$, K is the internal degree of freedom, i.e. $K = (4 - 2\gamma)/(\gamma - 1)$ for two-dimensional flows, and γ is the specific heat ratio.

In the continuum regime, the gas distribution function can be expanded as

$$f = g - \tau D_{\mathbf{u}} g + \tau D_{\mathbf{u}} (\tau D_{\mathbf{u}}) g - \tau D_{\mathbf{u}} [\tau D_{\mathbf{u}} (\tau D_{\mathbf{u}}) g] + \dots,$$

where $D_{\mathbf{u}} = \partial/\partial t + \mathbf{u} \cdot \nabla$. The corresponding macroscopic equations can be derived by truncating on different order of τ . For example, when the zeroth-order truncation is taken, i.e. $f = g$, the Euler equations can be derived. When the first-order truncation is used,

$$f = g - \tau(ug_x + vg_y + g_t), \quad (6)$$

the Navier-Stokes equations can be derived with $\tau = \mu/p$. The difficulties for the development of a reliable gas-kinetic scheme is the possible discontinuity of flow variables at the cell interface, where the above Chapman-Enskog expansion cannot be used directly for the flux evaluation, and the time evolution solution of the gas distribution function at the cell interface has to be constructed properly from a piecewise discontinuous initial condition.

Based on the conservation laws in a discretized space of control volume $S_{ij} = [x_i - \Delta x/2, x_i + \Delta x/2] \times [y_j - \Delta y/2, y_j + \Delta y/2]$, the semi-discrete form of finite volume scheme can be obtained as

$$\frac{d\mathbf{W}_{ij}}{dt} = -\frac{1}{\Delta x}(\mathbf{F}_{i+1/2,j}(t) - \mathbf{F}_{i-1/2,j}(t)) - \frac{1}{\Delta y}(\mathbf{G}_{i,j+1/2}(t) - \mathbf{G}_{i,j-1/2}(t)), \quad (7)$$

where $\mathbf{W}_{ij} = [\rho, \rho U, \rho V, \rho E]^T$ are the cell-averaged conservative variables. $\mathbf{F}_{i\pm 1/2,j}(t)$ and $\mathbf{G}_{i,j\pm 1/2}(t)$ are the time-dependent numerical fluxes across the cell interfaces in x and y directions respectively. The fluxes can be obtained by a time-dependent gas distribution function f at the corresponding cell interface. To achieve the accuracy in space, the Gaussian quadrature is used. Taking the numerical fluxes in x directions $\mathbf{F}_{i+1/2,j}(t)$, for example,

$$\mathbf{F}_{i+1/2,j}(t) = \frac{1}{\Delta y} \int_{y_{j-1/2}}^{y_{j+1/2}} \mathbf{F}_{i+1/2}(y, t) dy = \sum_{\ell=1}^2 \omega_{\ell} \mathbf{F}_{i+1/2,j_{\ell}}(t), \quad (8)$$

two Gaussian quadrature points $y_{j_{\ell}} = y_j + \frac{(-1)^{\ell-1}}{2\sqrt{3}}\Delta y$, $\ell = 1, 2$, and the corresponding weights $\omega_1 = \omega_2 = 1/2$ are employed in this paper, which yields fourth-order accuracy in space. $\mathbf{F}_{i+1/2,j_{\ell}}(t)$, $\ell = 1, 2$, are numerical fluxes at the Gaussian quadrature points,

$$\mathbf{F}_{i+1/2,j_{\ell}}(t) = \int \boldsymbol{\psi} u f(x_{i+1/2}, y_{\ell}, t, u, v, \xi) d\Xi, \quad (9)$$

where $f(x_{i+1/2}, y_{\ell}, t, u, v, \xi)$, $\ell = 1, 2$, are the gas distribution function at the Gaussian points. To obtain the numerical fluxes, the integral solution of BGK equation Eq.(4) at point $(x_{i+1/2}, y_{\ell})$ and time t is used,

$$f(x_{i+1/2}, y_{\ell}, t, u, v, \xi) = \frac{1}{\tau} \int_0^t g(x', y', t', u, v, \xi) e^{-(t-t')/\tau} dt' + e^{-t/\tau} f_0(-ut, -vt, u, v, \xi), \quad (10)$$

where $(x_{i+1/2}, y_{\ell}) = (0, 0)$ for the simplification of the notation, $x = x' + u(t - t')$ and $y = y' + v(t - t')$ are the trajectory of particles. f_0 is the initial gas distribution function at time $t = 0$, and g is the corresponding equilibrium state.

In the integral solution Eq.(10), the initial gas distribution function can be constructed as

$$f_0 = f_0^l(x, y, u, v)H(x) + f_0^r(x, y, u, v)(1 - H(x)), \quad (11)$$

where $H(x)$ is the Heaviside function, f_0^l and f_0^r are the initial gas distribution functions on the left and right side of one cell interface, which can be determined by the corresponding

macroscopic variables. The initial gas distribution function f_0^k , $k = l, r$, is constructed as

$$f_0^k = g^k (1 + a^k x + b^k y - \tau(a^k u + b^k v + A^k)),$$

where g^l and g^r are the Maxwellian distribution functions on the left and right hand sides of a cell interface, and they can be determined by the corresponding conservative variables \mathbf{W}^l and \mathbf{W}^r . The coefficients a^l , a^r , b^l , b^r are related to the spatial derivatives in normal and tangential directions, which can be obtained from the corresponding derivatives of the initial macroscopic variables,

$$\langle a^l \rangle = \partial \mathbf{W}^l / \partial x, \langle a^r \rangle = \partial \mathbf{W}^r / \partial x, \langle b^l \rangle = \partial \mathbf{W}^l / \partial y, \langle b^r \rangle = \partial \mathbf{W}^r / \partial y,$$

where $\langle \dots \rangle$ means the moments of the Maxwellian distribution function,

$$\langle \dots \rangle = \int \psi(\dots) g d\Xi.$$

The non-equilibrium parts on the Chapman-Enskog expansion have no net contribution to the conservative variables,

$$\langle a^l u + b^l v + A^l \rangle = 0, \quad \langle a^r u + b^r v + A^r \rangle = 0,$$

and therefore the coefficients A^l and A^r , related to time derivatives, can be obtained. After the determination of f_0 , the equilibrium state g around the cell interface is modeled as,

$$g = g_0 (1 + \bar{a}x + \bar{b}y + \bar{A}t), \quad (12)$$

where g_0 is the local equilibrium at point $(x_{i+1/2}, y_\ell)$ and can be determined by the compatibility condition,

$$\begin{aligned} \int \psi g_0 d\Xi &= \mathbf{W}_0 = \int_{u>0} \psi g^l d\Xi + \int_{u<0} \psi g^r d\Xi, \\ \int \psi \bar{a} g_0 d\Xi &= \partial \mathbf{W}_0 / \partial x = \int_{u>0} \psi a^l g^l d\Xi + \int_{u<0} \psi a^r g^r d\Xi, \\ \int \psi \bar{b} g_0 d\Xi &= \partial \mathbf{W}_0 / \partial y = \int_{u>0} \psi b^l g^l d\Xi + \int_{u<0} \psi b^r g^r d\Xi, \end{aligned} \quad (13)$$

and

$$\langle \bar{a}u + \bar{b}v + \bar{A} \rangle = 0.$$

After constructing the initial gas distribution function f_0 and the equilibrium state g , and substituting Eq.(11) and Eq.(12) into Eq.(10), the time-dependent distribution function

$f(x_{i+1/2}, y_\ell, t, u, v, \xi)$ at a cell interface can be expressed as,

$$\begin{aligned}
f(x_{i+1/2, j_\ell}, t, u, v, \xi) = & (1 - e^{-t/\tau})g_0 + [(t + \tau)e^{-t/\tau} - \tau](\bar{a}u + \bar{b}v)g_0 \\
& + (t - \tau + \tau e^{-t/\tau})\bar{A}g_0 \\
& + e^{-t/\tau}g^r[1 - (\tau + t)(a^r u + b^r v) - \tau A^r]H(u) \\
& + e^{-t/\tau}g^l[1 - (\tau + t)(a^l u + b^l v) - \tau A^l](1 - H(u)). \tag{14}
\end{aligned}$$

The collision time τ in Eq.(14) is defined by

$$\tau = \frac{\mu}{p} + c_2 \left| \frac{p_l - p_r}{p_l + p_r} \right| \Delta t,$$

for viscous flow computation, where p_l and p_r are the pressures on the left and right sides of the cell interface, and p is the pressure at the interface from the equilibrium state. Here Δt is the time step. For inviscid flow, the τ is given by

$$\tau = c_1 \Delta t + c_2 \left| \frac{p_l - p_r}{p_l + p_r} \right| \Delta t,$$

where $c_1 = 0.01$, $c_2 = 1 \sim 5$.

2.2.2. Two-stage fourth-order temporal discretization

The two-stage fourth-order temporal discretization, originally developed for the generalized Riemann problem (GRP) solver [20], has been applied to GKS [28]. A fourth-order time-accurate GKS can be constructed using the second-order flux function Eq.(14). For the time-dependent equations,

$$\frac{\partial \mathbf{W}}{\partial t} = \mathcal{L}(\mathbf{W}), \tag{15}$$

with the initial condition at t_n ,

$$\mathbf{W}(t = t_n) = \mathbf{W}^n, \tag{16}$$

where \mathcal{L} is the spatial operator of flux obtained in Eq.(7), a fourth-order temporal accurate solution for $\mathbf{W}(t)$ at $t = t_n + \Delta t$ can be updated by,

$$\mathbf{W}^* = \mathbf{W}^n + \frac{1}{2}\Delta t \mathcal{L}(\mathbf{W}^n) + \frac{1}{8}\Delta t^2 \frac{\partial}{\partial t} \mathcal{L}(\mathbf{W}^n). \tag{17}$$

$$\mathbf{W}^{n+1} = \mathbf{W}^n + \Delta t \mathcal{L}(\mathbf{W}^n) + \frac{1}{6}\Delta t^2 \left(\frac{\partial}{\partial t} \mathcal{L}(\mathbf{W}^n) + 2 \frac{\partial}{\partial t} \mathcal{L}(\mathbf{W}^*) \right). \tag{18}$$

The detailed proof is given in [20].

The numerical fluxes and their time derivatives in the above equations, such as $\mathcal{L}(W_i^n)$

and $\frac{\partial}{\partial t}\mathcal{L}(W_i^n)$, are determined by

$$\begin{aligned}\mathcal{L}(\mathbf{W}_{i,j}^n) &= -\frac{1}{\Delta x}[(\mathbf{F})_{i+1/2,j}(\mathbf{W}^n, t_n) - (\mathbf{F})_{i-1/2,j}(\mathbf{W}^n, t_n)] \\ &\quad -\frac{1}{\Delta y}[(\mathbf{G})_{i,j+1/2}(\mathbf{W}^n, t_n) - (\mathbf{G})_{i,j-1/2}(\mathbf{W}^n, t_n)], \\ \mathcal{L}_t(\mathbf{W}_{i,j}^n) &= -\frac{1}{\Delta x}[\partial_t(\mathbf{F})_{i+1/2,j}(\mathbf{W}^n, t_n) - \partial_t(\mathbf{F})_{i-1/2,j}(\mathbf{W}^n, t_n)] \\ &\quad -\frac{1}{\Delta y}[\partial_t(\mathbf{G})_{i,j+1/2}(\mathbf{W}^n, t_n) - \partial_t(\mathbf{G})_{i,j-1/2}(\mathbf{W}^n, t_n)].\end{aligned}\tag{19}$$

Similarly, the time derivatives for the intermediate state can be obtained,

$$\begin{aligned}\mathcal{L}_t(\mathbf{W}_{i,j}^*) &= -\frac{1}{\Delta x}[\partial_t(\mathbf{F})_{i+1/2,j}(\mathbf{W}^*, t_*) - \partial_t(\mathbf{F})_{i-1/2,j}(\mathbf{W}^*, t_*)] \\ &\quad -\frac{1}{\Delta y}[\partial_t(\mathbf{G})_{i,j+1/2}(\mathbf{W}^*, t_*) - \partial_t(\mathbf{G})_{i,j-1/2}(\mathbf{W}^*, t_*)].\end{aligned}\tag{20}$$

In the gas-kinetic scheme, the flux Eq.(8) is a complicated function of time. To obtain the time derivatives of the flux function used in the above two-stage fourth-order framework, the flux function is approximated as a linear function of time within a time interval. The time-dependent flux can be expanded as,

$$\mathbf{F}_{i+1/2,j}(\mathbf{W}^n, t) = \mathbf{F}_{i+1/2,j}^n + \partial_t \mathbf{F}_{i+1/2,j}^n (t - t_n), t \in [t_n, t_n + \Delta t].\tag{21}$$

To get coefficients $\mathbf{F}_{i+1/2,j}^n$ and $\partial_t \mathbf{F}_{i+1/2,j}^n$, the following notation of Eq.(8) is introduced,

$$\mathbb{F}_{i+1/2,j}(\mathbf{W}^n, \delta) = \int_{t_n}^{t_n+\delta} \mathbf{F}_{i+1/2,j}(\mathbf{W}^n, t) dt = \sum_{\ell=1}^2 \omega_\ell \int_{t_n}^{t_n+\delta} \int u \psi f(x_{i+1/2,j_\ell}, t, u, v, \xi) d\Xi dt.$$

Take δ as Δt and $\Delta t/2$, we have,

$$\begin{aligned}\mathbf{F}_{i+1/2,j}(\mathbf{W}^n, t_n) \Delta t + \frac{1}{2} \partial_t \mathbf{F}_{i+1/2,j}(\mathbf{W}^n, t_n) \Delta t^2 &= \mathbb{F}_{i+1/2,j}(\mathbf{W}^n, \Delta t), \\ \frac{1}{2} \mathbf{F}_{i+1/2,j}(\mathbf{W}^n, t_n) \Delta t + \frac{1}{8} \partial_t \mathbf{F}_{i+1/2,j}(\mathbf{W}^n, t_n) \Delta t^2 &= \mathbb{F}_{i+1/2,j}(\mathbf{W}^n, \Delta t/2).\end{aligned}$$

Solving the above linear system, and we can obtain the expression of coefficients

$$\begin{aligned}\mathbf{F}_{i+1/2,j}(\mathbf{W}^n, t_n) &= (4\mathbb{F}_{i+1/2,j}(\mathbf{W}^n, \Delta t/2) - \mathbb{F}_{i+1/2,j}(\mathbf{W}^n, \Delta t))/\Delta t, \\ \partial_t \mathbf{F}_{i+1/2,j}(\mathbf{W}^n, t_n) &= 4(\mathbb{F}_{i+1/2,j}(\mathbf{W}^n, \Delta t) - 2\mathbb{F}_{i+1/2,j}(\mathbf{W}^n, \Delta t/2))/\Delta t^2.\end{aligned}$$

Similarly, the coefficients for the intermediate state $\mathbf{F}_{i+1/2,j}(\mathbf{W}^*, t_*)$, $\partial_t \mathbf{F}_{i+1/2,j}(\mathbf{W}^*, t_*)$ can be determined as well. The fluxes in y-direction can be obtained through the same method. Then, the intermediate states $\mathbf{W}_{i,j}^*$ are updated by Eq.(17) and Eq.(19). The final states

\mathbf{W}_{ij}^{n+1} in Eq.(18) are determined through Eq.(19) and Eq.(20).

2.3. WENO5-AO-HLLC scheme

2.3.1. HLLC Riemann solver

The HLLC Riemann solver [36] is used to obtain the inviscid flux in the current WENO5-AO-HLLC scheme. Consider the following Riemann problem,

$$\mathbf{W}_t + \mathbf{F}_x(\mathbf{W}) = 0,$$

with the initial condition,

$$\mathbf{W}(x, 0) = \begin{cases} \mathbf{W}_L, & x < 0, \\ \mathbf{W}_R, & x > 0, \end{cases}$$

where \mathbf{W}_L and \mathbf{W}_R are the initial interface values. For the two-dimensional Euler equations, the conservative variables \mathbf{W} and the corresponding fluxes \mathbf{F} are,

$$\mathbf{W} = [\rho, \rho U, \rho V, \rho E]^T, \quad \mathbf{F} = [\rho U, \rho U^2 + p, \rho UV, U(\rho E + p)]^T.$$

HLLC solver is an approximate Riemann solver, which consists of four constant states. Assume that the speeds of the slowest and fastest wave are S_L and S_R , and the speed of the middle shear wave is S_* . Then, the HLLC solver can be written as follows,

$$\mathbf{W}(x, t) = \begin{cases} \mathbf{W}_L, & \frac{x}{t} \leq S_L, \\ \mathbf{W}_{*L}, & S_L \leq \frac{x}{t} \leq S_*, \\ \mathbf{W}_{*R}, & S_* \leq \frac{x}{t} \leq S_R, \\ \mathbf{W}_R, & \frac{x}{t} \geq S_R, \end{cases} \quad (22)$$

and the corresponding numerical flux can be defined as,

$$\mathbf{F}_{x+1/2} = \begin{cases} \mathbf{F}_L, & 0 \leq S_L, \\ \mathbf{F}_{*L}, & S_L \leq 0 \leq S_*, \\ \mathbf{F}_{*R}, & S_* \leq 0 \leq S_R, \\ \mathbf{F}_R, & 0 \geq S_R, \end{cases} \quad (23)$$

where $\mathbf{F}_{*K} = \mathbf{F}_K + S_L(\mathbf{W}_{*K} - \mathbf{W}_K)$, $K = L, R$. The \mathbf{W}_{*K} , $K = L, R$, is given by,

$$\mathbf{W}_{*K} = \rho_K \left(\frac{S_K - U_K}{S_K - S_*} \right) \begin{bmatrix} 1 \\ S_* \\ V_K \\ \frac{E_K}{\rho_K} + (S_* - U_K) \left[S_* + \frac{p_K}{\rho_K(S_K - U_K)} \right] \end{bmatrix}, \quad (24)$$

where S_* is related to the speeds S_L and S_R , namely

$$S_* = \frac{p_R - p_L + \rho_L U_L (S_L - U_L) - \rho_R U_R (S_R - U_R)}{\rho_L (S_L - U_L) - \rho_R (S_R - U_R)}.$$

There are many methods to estimate wave speeds S_L and S_R , and a pressure-based wave speed estimate method proposed by Toro is adopted in the current work [34]. Firstly, we need to estimate p_* , the pressure of the region $x/t \in [S_L, S_R]$. Based on the Two-Rarefaction Riemann solver (TRRS), the estimated p_* is

$$p_* = \left[\frac{a_L + a_R - \frac{\gamma-1}{2} (U_R - U_L)}{a_L/p_L^z + a_R/p_R^z} \right]^{1/z}$$

where $z = (\gamma - 1) / (2\gamma)$, and γ is the specific heat ratio. Then, the speeds S_L and S_R are coming from the exact wave-speed relations in the exact Riemann solver,

$$S_L = U_L - a_L q_L, \quad S_R = U_R - a_R q_R,$$

where a_L, a_R are the sound speeds of initial left and right state, and $q_K, K = L, R$, are

$$q_K = \begin{cases} 1, & p_* \leq p_K, \\ \left[1 + \frac{\gamma+1}{2\gamma} (p_*/p_K - 1) \right]^{1/2}, & p_* > p_K. \end{cases}$$

2.3.2. Viscous flux

For viscous flow problems, the viscous fluxes in Navier-Stokes equations are needed. To calculate the viscous fluxes in the current WENO5-AO-HLLC scheme, both the conservative variables $Q_{i+1/2}$ and the corresponding derivatives $(Q_x)_{i+1/2}$ at the cell interface need to be constructed by the cell averaged conservative variables \bar{Q} . In this paper, a sixth-order central difference method is applied for the calculation of viscous fluxes. The conservative variables can be written as follows,

$$Q_{i+1/2} = \frac{1}{60} (\bar{Q}_{i-2} - 8\bar{Q}_{i-1} + 37\bar{Q}_i + 37\bar{Q}_{i+1} - 8\bar{Q}_{i+2} + \bar{Q}_{i+3}),$$

and the corresponding derivatives are,

$$(Q_x)_{i+1/2} = \frac{1}{180\Delta x} (-2\bar{Q}_{i-2} + 25\bar{Q}_{i-1} - 245\bar{Q}_i + 245\bar{Q}_{i+1} - 25\bar{Q}_{i+2} + 2\bar{Q}_{i+3}).$$

For two-dimensional problems, the dimension-by-dimension strategy is adopted [42, 15]. The reconstructed value $Q_{i+1/2, j_l}$ at the Gaussian quadrature point j_l , the corresponding normal derivative $(Q_x)_{i+1/2, j_l}$, and tangential derivative $(Q_y)_{i+1/2, j_l}$ can be obtained by the fourth-order polynomial $p^{r^5}(y)$ based on the above $Q_{i+1/2}$ and $(Q_x)_{i+1/2}$. Then, all terms in

the viscous fluxes can be fully determined. A similar procedure can be easily extended to three-dimensional problems. To improve the robustness of WENO5-AO-HLLC scheme, the conservative variables at the cell interface $Q_{i+1/2}$ are obtained by simple averaging of the left and right interface values of WENO5-AO reconstruction in some challenging cases.

2.3.3. Time marching method

Considering the fourth-order temporal accuracy in WENO5-AO-GKS scheme, the classical fourth-order Runge-Kutta method (RK4) is adopted for time integration in WENO5-AO-HLLC scheme for achieving the 4th-order temporal accuracy. The RK4 time marching method reads,

$$\begin{aligned}\mathbf{W}^1 &= \mathbf{W}^n + \frac{1}{2}\Delta t\mathcal{L}(\mathbf{W}^n), \\ \mathbf{W}^2 &= \mathbf{W}^n + \frac{1}{2}\Delta t\mathcal{L}(\mathbf{W}^1), \\ \mathbf{W}^3 &= \mathbf{W}^n + \Delta t\mathcal{L}(\mathbf{W}^2), \\ \mathbf{W}^{n+1} &= \mathbf{W}^n + \frac{1}{6}(\Delta t\mathcal{L}(\mathbf{W}^n) + 2\Delta t\mathcal{L}(\mathbf{W}^1) + 2\Delta t\mathcal{L}(\mathbf{W}^2) + \Delta t\mathcal{L}(\mathbf{W}^3)),\end{aligned}$$

with \mathcal{L} defined in Eq.(19).

3. Numerical performance

In the following test cases, for the inviscid flow the time step is determined by,

$$\Delta t = \text{CFL} \times \frac{\Delta x}{(|\mathbf{U}| + C)_{\text{Max}}},$$

where C is sound speed. For viscous flow, the time step is given by,

$$\Delta t = \text{CFL} \times \text{Min} \left[\frac{\Delta x}{(|\mathbf{U}| + C)_{\text{Max}}}, \frac{\rho\Delta x^2}{4\mu} \right].$$

3.1. 1-D test case

3.1.1. Titarev-Toro problem

Titarev-Toro problem is an inviscid flow problem with a shock wave impinging into a high-frequency density perturbation [32]. This problem consists of a main shock, a high gradient smooth post-shock region and multiple shocklets developed later. To represent these flow structures, a high-order scheme is needed. The initial condition is given by,

$$(\rho, U, p) = \begin{cases} (1.515695, 0.523346, 1.80500), & -5.0 \leq x \leq -4.5, \\ (1 + 0.1\sin(20\pi x), 0.0, 1.0), & -4.5 < x \leq 5.0. \end{cases}$$

The computational domain is $[-5, 5]$ with a mesh of 1000 cells. Two CFL numbers, 0.5 and 1.0, are employed for both WENO5-AO-GKS and WENO5-AO-HLLC, and the results at

the output time $t = 5.0$ are presented in Figure 1 and Figure 2, respectively. The results show that WENO5-AO-GKS scheme is more accurate than WENO5-AO-HLLC scheme at both CFL numbers, especially in the region behind the interaction of shock wave with the smooth acoustic wave. These results may indicate the importance of time accurate flux in the simulation of high frequency unsteady flow.

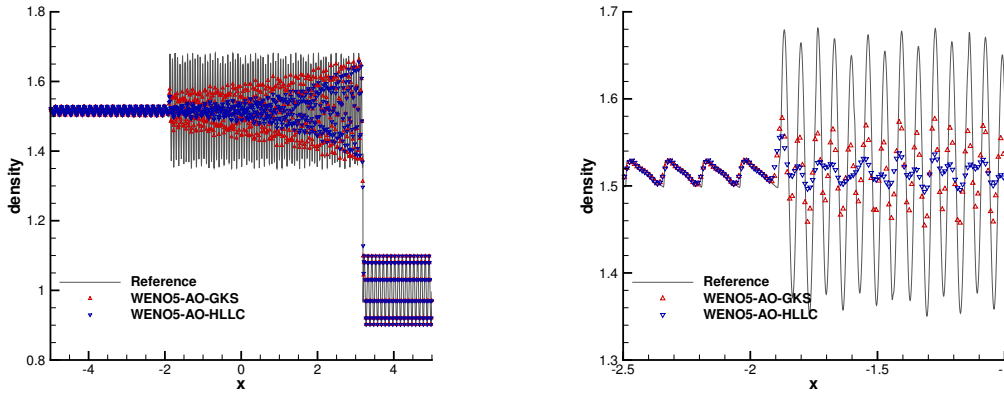


Figure 1: Titarev-Toro problem by WENO5-AO-GKS scheme and WENO5-AO-HLLC scheme. Density distribution with mesh number 1000 at $t = 5.0$. Left figure shows the whole domain; right figure shows the enlarged domain. The CFL number is 0.5.

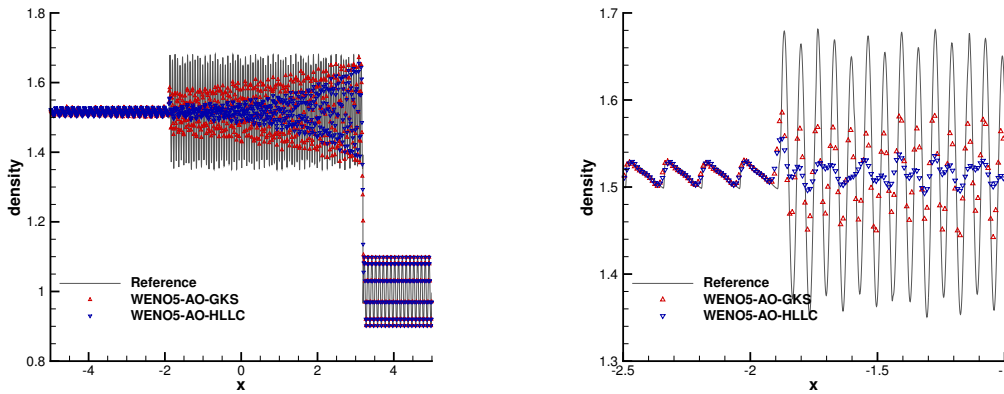


Figure 2: Titarev-Toro problem by WENO5-AO-GKS scheme and WENO5-AO-HLLC scheme. Density distribution with mesh number 1000 at $t = 5.0$. Left figure shows the whole domain; right figure shows the enlarged domain. The CFL number is 1.

3.1.2. Le Blanc problem

Le Blanc problem is a class of 1-D Riemann problems with initially high ratios for density and pressure [31]. Therefore, an extremely strong rarefaction wave is generated in the high-

pressure region. The initial condition here is chosen as,

$$(\rho, U, p) = \begin{cases} (10^M, 0, 10^M), & 0 \leq x \leq 0.3, \\ (1, 0, 1), & 0.3 < x \leq 1. \end{cases}$$

Here Le Blanc problem with initial pressure ratio 10^3 and 10^4 was calculated by WENO5-AO-GKS scheme and WENO5-AO-HLLC scheme, and the profiles of density, temperature, and pressure at $t = 0.12$ are presented in Figure 3. For this case, CFL number is 0.5. For both two schemes, there exist discrepancy in the vicinity of the shock wave, which has also been observed in the previous research, especially in the coarse mesh case [31]. Both schemes present a similar performance in this case.

3.1.3. Noh problem

Noh problem consists of two strong shocks moving from center to left and right side respectively [25]. The initial condition is as follows,

$$(\rho, U, p) = \begin{cases} (1, 1, 10^{-6}), & 0 \leq x \leq 0.5, \\ (1, -1, 10^{-6}), & 0.5 < x \leq 1. \end{cases}$$

The computational domain is $[0, 1]$, which is covered by 400 cells. In this problem, the specific heat ratio is $\gamma = 5/3$. The output time is $t = 1.0$. The results are presented in Figure 4. It is worth noting that WENO5-AO-HLLC scheme blows up for this problem while WENO5-AO-GKS scheme can work well. Besides, as a comparison, the WENO5-AO-LF scheme is adopted for this problem. The WENO5-AO-LF scheme means that, only HLLC solver in WENO5-AO-HLLC scheme is replaced by Lax-Friedrich solver. The results show that both two schemes can resolve the shock very well, although the density profiles exist a weak dip at the central region for both schemes. Besides, the result of WENO5-AO-GKS scheme shows a weaker dip.

3.2. 2-D tests

3.2.1. Forward step problem

The forward step problem proposed by Woodward and Colella [37] is an inviscid test case. A uniform flow with $Ma = 3$ blows towards a wind tunnel containing a step. This wind tunnel size, is $[0, 3] \times [0, 1]$; the step is located at 0.6 from the left and has 0.2 high. The initial condition can be described as,

$$(\rho, U, V, p) = (1, 3, 0, 1/\gamma),$$

where $\gamma = 1.4$. The supersonic inlet and outlet boundary condition is employed for the left and right boundary respectively, while other boundaries are set as reflective boundary conditions. It is worth remarking that, the ghost cells near the corner of the step $[0.6, 0.2]$ are given as follows: velocity U is given by the value obtained through applying the reflective boundary condition for the upper flow region; velocity V is given by the value obtained

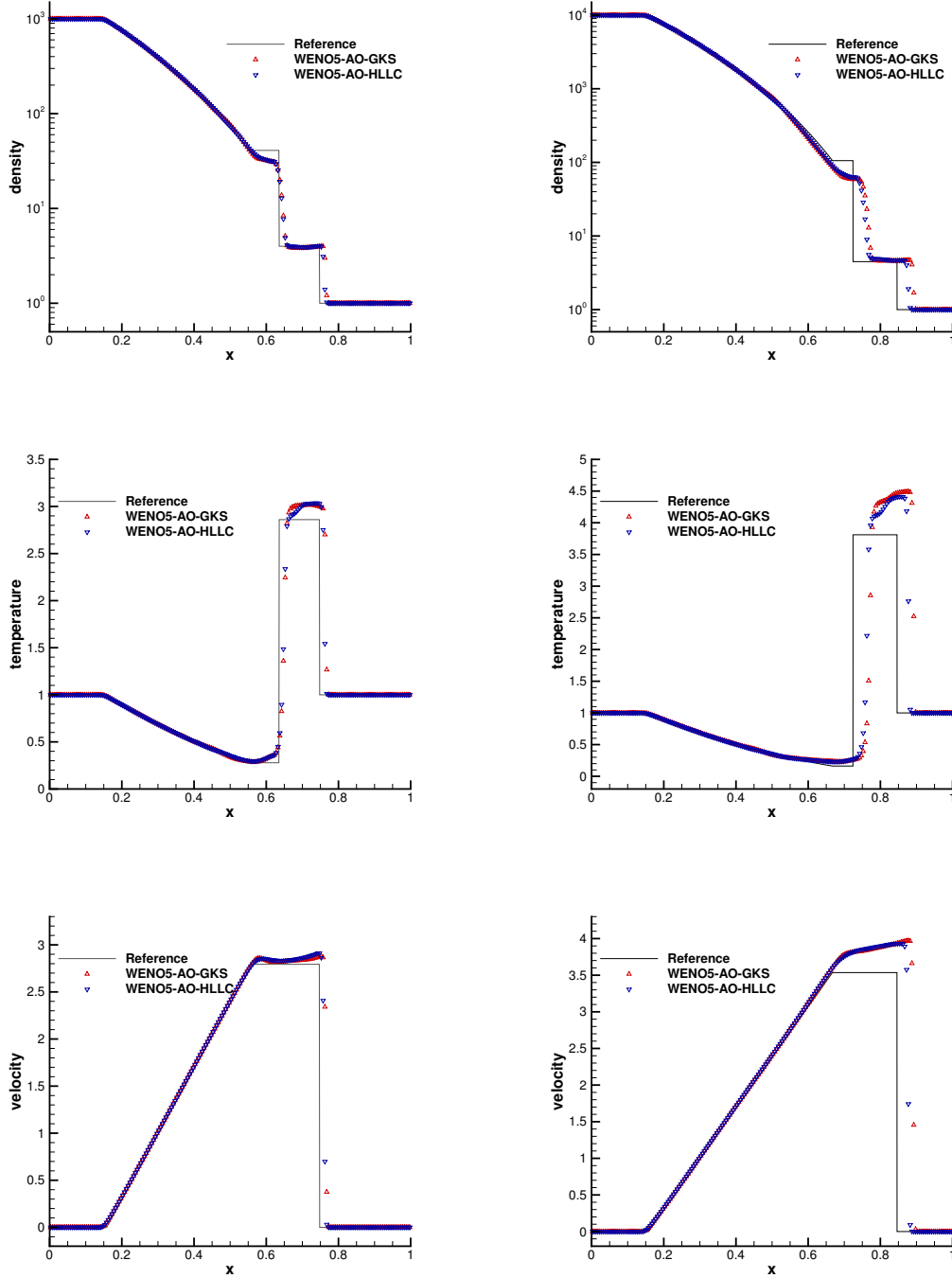


Figure 3: Le Blanc problem with initial pressure ratio 10^3 (left three figures) and 10^4 (right three figures) by WENO5-AO-GKS scheme and WENO5-AO-HLLC scheme. For all figures, CFL number is 0.5, the mesh number is 200 and the output time is $t = 0.12$.

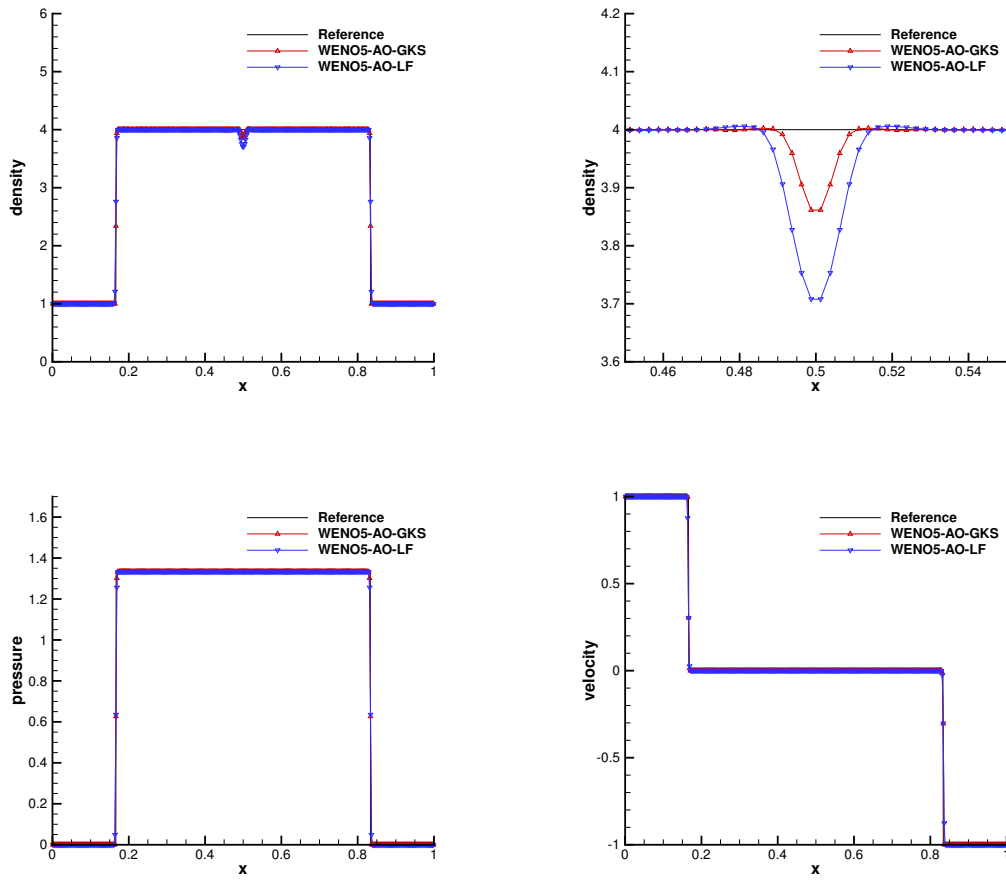


Figure 4: Noh problem by WENO5-AO-GKS scheme and WENO5-AO-LF scheme. The density, pressure, and velocity profiles respectively with CFL number 0.5 are shown. For all figures, the mesh number is 400 and the output time is $t = 1.0$. The WENO-AO-HLLC fails for this test case.

through applying reflective boundary condition for the left flow region; density ρ and pressure p are given by algebraically averaging the corresponding values obtained through the reflective boundary condition for the upper and left flow regions. The CFL number 0.8 is used. The results are shown in Figure 5, respectively. For each case, three values of the mesh size, $\Delta x = \Delta y = 1/120, 1/240, 1/360$, are taken, and the output time is $t = 4.0$. The results show that both WENO5-AO-GKS scheme and WENO5-AO-HLLC scheme perform well when adopting a fine mesh. In the top region, both the triple-point structure and the vortex sheet can be captured clearly.

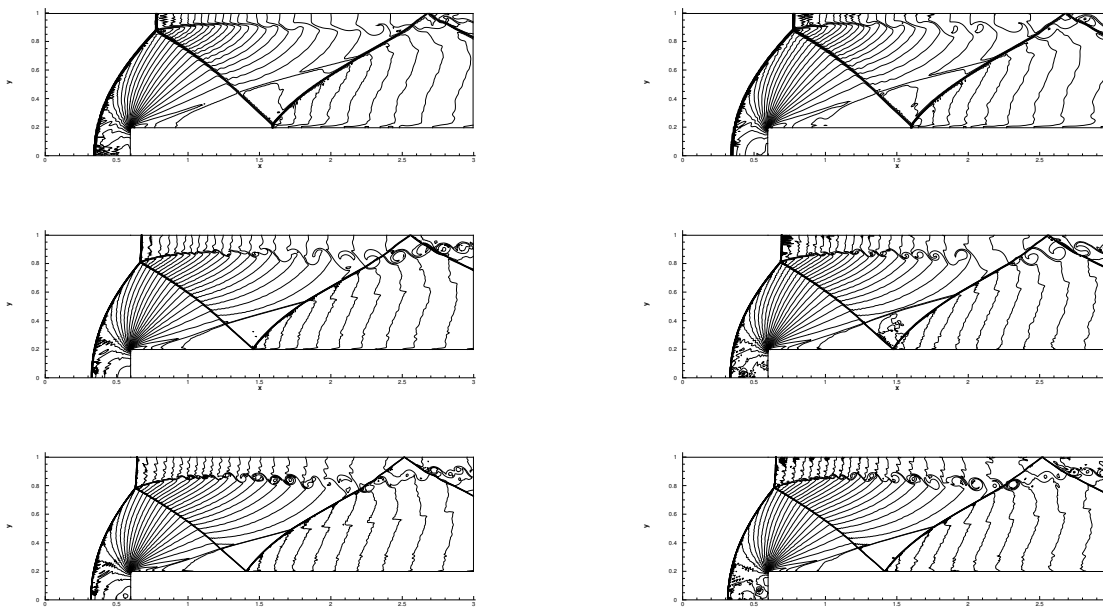


Figure 5: Mach 3 forward step problem by WENO5-AO-GKS scheme (left) and WENO5-AO-HLLC scheme (right). Density distribution with different mesh size at $t = 4.0$. The mesh size of the top figure, middle figure, and bottom figure are $1/120$, $1/240$, and $1/360$. The CFL number is 0.8 for both WENO-AO-GKS and WENO5-AO-HLLC. 30 equally spaced contours from 0.2 to 4.7 are plotted.

3.2.2. Laminar boundary layer

Laminar boundary layer is a standard test case for viscous flow [39]. A plane with the characteristic length $L = 100$ is placed from 0 to 100. The computation domain is $[-30, 100] \times [0, 80]$. Non-uniform mesh is adopted, which is shown in Figure 6. The mesh number is 120×32 . At the start point of plane, the minimal cell mesh Δx and Δy are 0.1 and 0.12 separately. The inlet flow is described by,

$$(\rho, U, V, p) = (1, 0.15, 0, 1/\gamma),$$

where $\gamma = 1.4$. In the case, kinematic viscosity coefficient is $\nu = 1.5 \times 10^{-4}$, and thus $Re = U_\infty L/\nu = 1.0 \times 10^5$ and $Ma = 0.15$. Besides, the adiabatic non-slip boundary

condition is adopted on the plate, while the symmetric slip boundary condition is used for the bottom boundary of $[-30, 0]$. The outflow boundary condition is given at the right boundary. The non-reflecting boundary condition is imposed on other boundaries.

The results are presented in Figure 7, where the non-dimensional length $ys = y\sqrt{Re}/x$, and the non-dimensional velocity $us = U/U_\infty$, $vs = V\sqrt{Re_x}/U_\infty$, respectively. The values in the legend represent the location x/L . From the results, both WENO5-AO-GKS and WENO5-AO-HLLC are capable of capturing the velocity profile well in the boundary layer with several mesh cells. Close to the leading edge, WENO5-AO-GKS gives a slightly better vs solution than WENO5-AO-HLLC at the location $x/L = 0.050$.

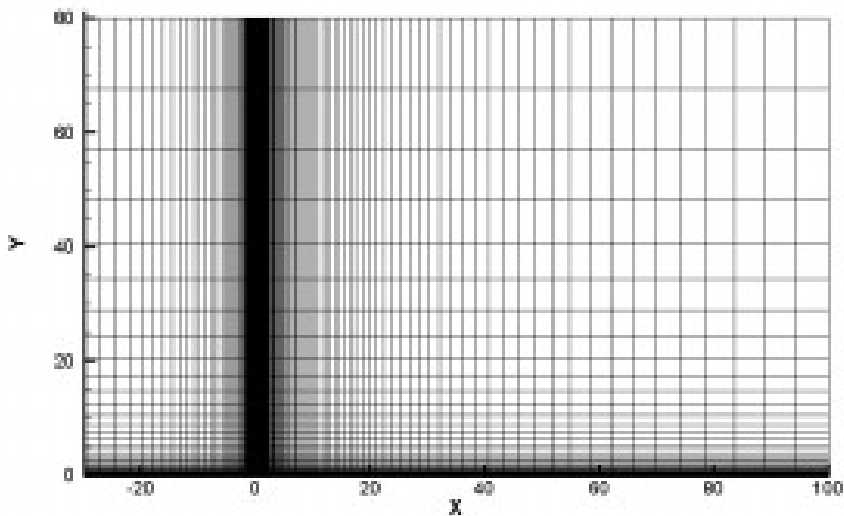


Figure 6: Mesh with 120×32 cells for laminar boundary layer case.

3.2.3. Double shear layer

Double shear layer is a viscous problem involving a pair of doubly-periodic shear layers [5]. When the numerical method is not enough to resolve the flow field, non-physical vortices will appear in the evolution stage. The “thin” shear layer problem is studied in [5], and the initial U velocity is given by,

$$U = \begin{cases} \tanh(k(y - 0.25)), & 0 \leq y \leq 0.5, \\ \tanh(k(0.75 - y)), & 0.5 < y \leq 1, \end{cases}$$

and the initial V velocity, density, and pressure are given as follows,

$$V = \delta \sin(2\pi x), \quad \rho = 1, \quad p = \frac{\rho U^2}{Ma^2 \gamma},$$

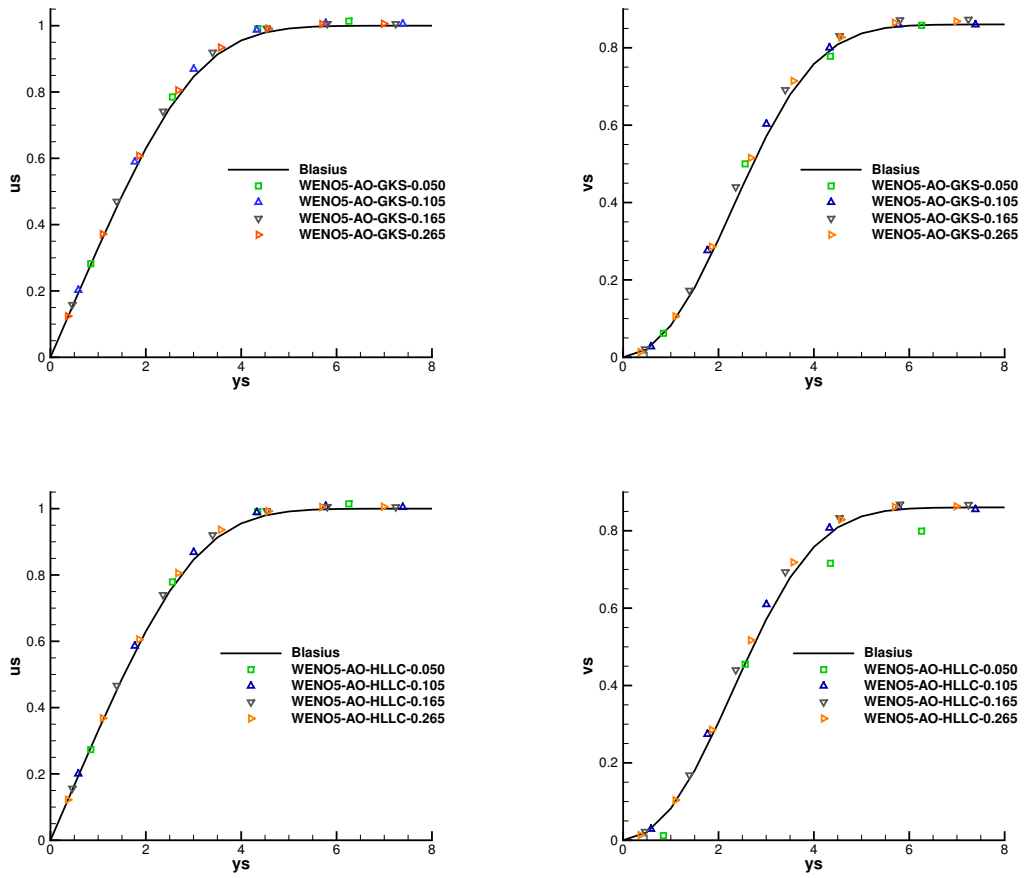


Figure 7: Laminar boundary layer by WENO5-AO-GKS scheme (top two) and WENO5-AO-HLLC scheme (bottom two). For all figures, $Re = 1.0 \times 10^5$, $Ma = 0.15$, CFL number is 0.5, and the mesh number is 120×32 .

where the shear layer width parameter $k = 100$, the perturbation size $\delta = 0.05$, the Mach number $Ma = 0.15$, and the specific heat ratio $\gamma = 1.4$. Besides, the kinetic viscosity is $\nu = 5.0 \times 10^{-5}$. Periodic boundary condition is employed for all boundaries. The computational domain is $[0, 1] \times [0, 1]$, and mesh number is 256×256 in this case. Linear reconstruction is employed for both schemes in this test.

The vorticity contours $\Omega = (\frac{\partial V}{\partial x} - \frac{\partial U}{\partial y})$ at $t = 0.8$ obtained by WENO5-AO-GKS and WENO5-AO-HLLC are presented in Figure 8. The results show that the vortex in the whole domain is captured by WENO5-AO-GKS. From the results of WENO5-AO-HLLC, the prominent vortex structures are well resolved and the spurious roll-ups appear, especially in the region near the location $(0.5, 0.75)$. These results indicate that WENO5-AO-GKS scheme has a slightly higher resolution than WENO5-AO-HLLC scheme even with the same reconstruction.

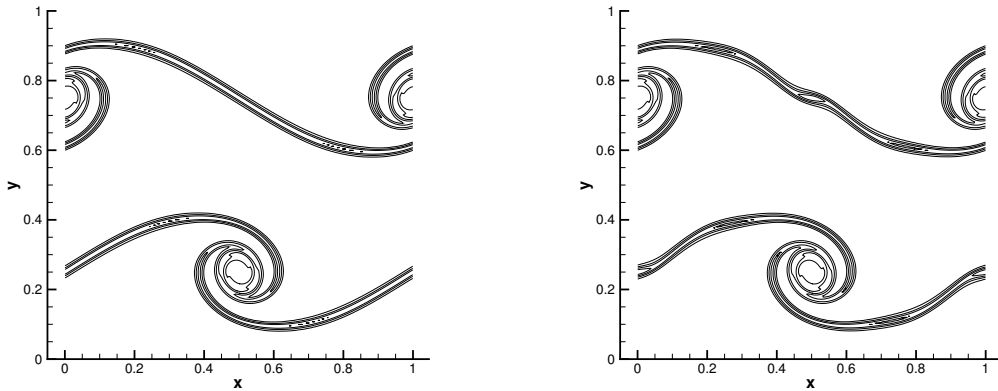


Figure 8: Two-dimensional double shear flow by WENO5-AO-GKS scheme (left) and WENO5-AO-HLLC scheme (right) : vorticity. The CFL number is 0.5, the output time is $t = 0.8$, and the mesh number is 256×256 . In figures, there are 10 equally spaced contours from -60 to 60.

3.2.4. Viscous shock tube

Viscous shock tube problem is a viscous flow problem with a strong shock [10]. The interaction of reflected shock from the right wall and the viscous boundary layer produces a series of complex flow structures, such as the typical λ -shape shock configuration. The initial condition is given by,

$$(\rho, U, V, p) = \begin{cases} (120, 0, 0, 120/\gamma), & 0 < x \leq 0.5, \\ (1.2, 0, 0, 1.2/\gamma), & 0.5 < x < 1, \end{cases}$$

where $\gamma = 1.4$, $Pr = 0.73$. The computational domain is $[0, 1] \times [0, 0.5]$. The simulation at $Re = 200$ is tested. The output time is $t = 1.0$. For the boundary condition, the upper boundary is asymmetric boundary, and others are the non-slip adiabatic wall. The density contours at $Re = 200$ are shown in Figure 9, where both WENO5-AO-GKS and

WENO5-AO-HLLC can capture the main flow structures. The λ -shape structure, the vortices within the boundary layer, and the slip line in the lower right region are captured clearly. The density profiles along the bottom wall are shown in Figure 10 with the local enlargement. The results show that both schemes have similar resolution. The results of WENO5-AO-GKS on both coarse and fine meshes seem to be closer than those of WENO5-AO-HLLC.

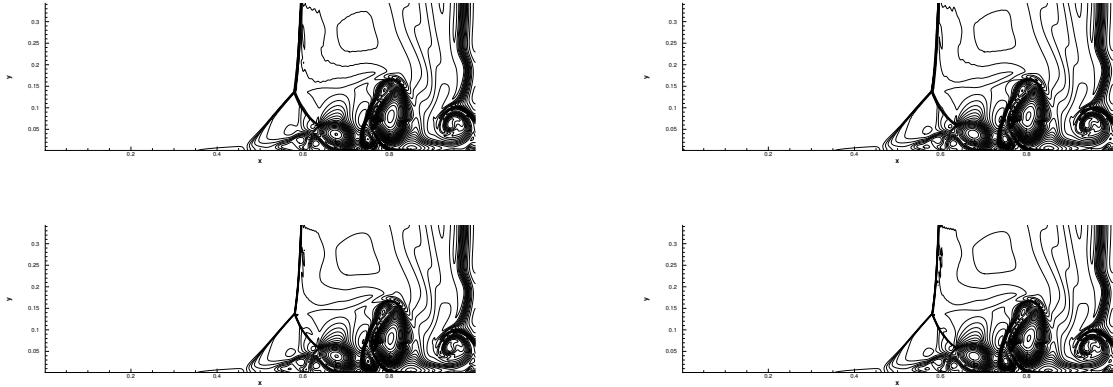


Figure 9: Viscous shock tube problem with $Re = 200$ by WENO5-AO-GKS scheme (left) and WENO5-AO-HLLC scheme (right): density distribution. For all cases, the CFL number is 0.2. For the top two figures, the mesh number is 500×250 ; and for the bottom two figures, the mesh number is 1000×500 . For all figures, there are 30 equally spaced contours from 20 to 130.

3.3. 3-D tests

3.3.1. Accuracy test

The three-dimensional advection of density perturbation is adopted for accuracy test. The initial condition is,

$$\begin{aligned} \rho(x, y, z) &= 1 + 0.2\sin(\pi(x + y + z)), \\ U(x, y, z) &= 1, V(x, y, z) = 1, W(x, y, z) = 1, p(x, y, z) = 1. \end{aligned}$$

The computational domain covers $[0, 2] \times [0, 2] \times [0, 2]$. Under the periodic boundary condition, the analytic solution is as follows,

$$\begin{aligned} \rho(x, y, z, t) &= 1 + 0.2\sin(\pi(x + y + z - t)), \\ U(x, y, z, t) &= 1, V(x, y, z, t) = 1, W(x, y, z, t) = 1, p(x, y, z, t) = 1. \end{aligned}$$

The L^1 error and convergence order of WENO5-AO-GKS and WENO5-AO-HLLC at $t = 2.0$ are shown in Table 1 and Table 2, respectively. The results show that the convergence orders of both schemes are higher than 4 in this test. The WENO5-AO-GKS scheme shows a slightly less absolute error than WENO5-AO-HLLC at different CFL number and mesh size.

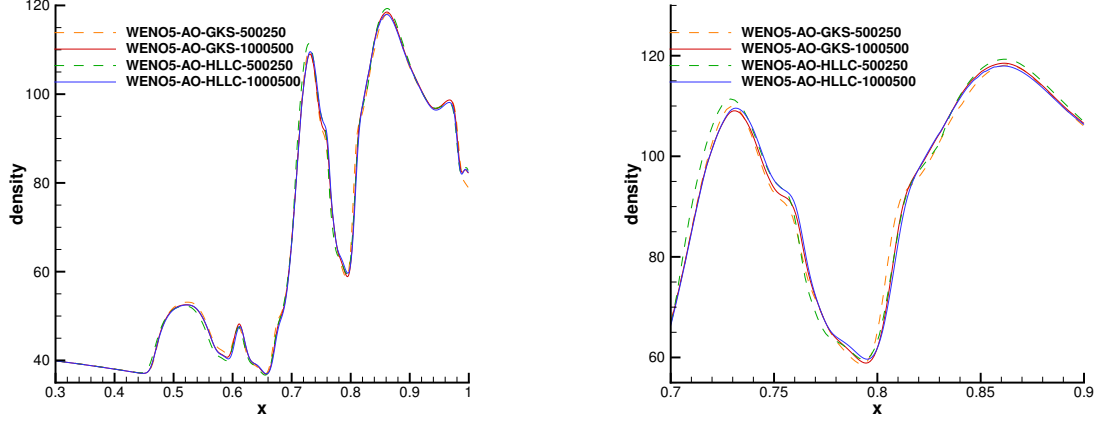


Figure 10: Viscous shock tube problem of $Re = 200$ by WENO5-AO-GKS scheme and WENO5-AO-HLLC scheme: density profile along the bottom wall ($y = 0$). The right is the enlarged figure. For all cases, the CFL number is 0.2.

CFL	0.20		0.60		1.00	
	L^1 Error	Order	L^1 Error	Order	L^1 Error	Order
Mesh						
$5 \times 5 \times 5$	4.574909e-02		3.704474e-02		5.481745e-02	
$10 \times 10 \times 10$	2.234252e-03	4.36	1.665667e-03	4.48	3.741869e-03	3.87
$20 \times 20 \times 20$	7.589204e-05	4.88	6.007786e-05	4.79	2.052167e-04	4.19
$40 \times 40 \times 40$	2.470600e-06	4.94	2.640903e-06	4.51	1.220770e-05	4.07
$80 \times 80 \times 80$	8.596794e-08	4.84	1.424737e-07	4.21	7.525234e-07	4.02

Table 1: 3-D accuracy test: L^1 Error and convergence order by WENO5-AO-GKS scheme with different CFL numbers.

CFL	0.20		0.60		1.00	
	L^1 Error	Order	L^1 Error	Order	L^1 Error	Order
Mesh						
$5 \times 5 \times 5$	5.960514e-02		6.192342e-02		7.703808e-02	
$10 \times 10 \times 10$	3.390217e-03	4.14	3.658550e-03	4.08	5.859740e-03	3.72
$20 \times 20 \times 20$	1.209088e-04	4.81	1.312929e-04	4.80	2.588044e-04	4.50
$40 \times 40 \times 40$	3.900971e-06	4.95	4.563747e-06	4.85	1.318523e-05	4.29
$80 \times 80 \times 80$	1.283506e-07	4.93	1.845443e-07	4.63	7.688684e-07	4.10

Table 2: 3-D accuracy test: L^1 Error and convergence order by WENO5-AO-HLLC scheme with different CFL numbers.

3.3.2. Compressible isotropic turbulence

The decaying compressible isotropic turbulence is a case to evaluate the robustness of different schemes [29, 6]. The definitions of flow variables are introduced first. The turbulent fluctuating velocity U' is,

$$U' = \left\langle \frac{U_1^2 + U_2^2 + U_3^2}{3} \right\rangle^{1/2},$$

where $\langle \dots \rangle$ means the space average over the whole computation domain. Then, turbulence Mach number Ma_t is given by,

$$Ma_t = \frac{\langle U_1^2 + U_2^2 + U_3^2 \rangle^{1/2}}{C} = \frac{\sqrt{3}U'}{C},$$

where C is the local sound speed. Taylor microscale λ is defined by,

$$\lambda^2 = \frac{(U')^2}{\langle (\partial U_1 / \partial x_1)^2 \rangle},$$

and the corresponding Taylor Reynolds number Re_λ is

$$Re_\lambda = \frac{\rho U' \lambda}{\mu},$$

where μ is the dynamic viscosity coefficient determined by

$$\mu = \mu_0 \left(\frac{T}{T_0} \right)^{0.76}.$$

In this case, the velocity spectrum is given by,

$$E(k) = A_0 k^4 e^{(-2k^2/k_0^2)},$$

where A_0 is the initial kinetic energy, k is the wave number, and k_0 is the peak value of k . The initial turbulent kinetic energy K_0 and the initial large-eddy-turnover time τ_0 can be obtained as follows,

$$K_0 = \frac{3A_0}{64} \sqrt{2\pi} k_0^5,$$

$$\tau_0 = \sqrt{\frac{32}{A_0}} (2\pi)^{1/4} k_0^{-7/2}.$$

The kinetic energy $K(t)$ and root-mean-square of density fluctuation $\rho_{rms}(t)$ are defined as

$$K(t) = \frac{\langle \rho U_1^2 + \rho U_2^2 + \rho U_3^2 \rangle}{2},$$

$$\rho_{rms}(t) = \sqrt{\langle (\rho - \bar{\rho})^2 \rangle}.$$

In this case, there are strong shocklets and shock-vortex interactions in the flow field, especially at a high turbulence Mach number Ma_t . Therefore, it is challenging for high-order scheme to simulate high Ma_t flow. The simulations will cover a wide range of Ma_t to compare the robustness of WENO5-AO-GKS and WENO5-AO-HLLC. The mesh adopted in this case is 128^3 . Other parameters take the values $Re_\lambda = 72$, $A_0 = 1.3 \times 10^{-4}$, and $k_0 = 8.0$.

The time history of normalized kinetic energy $K(t)/K_0$ and root-mean-square of density fluctuation $\rho_{rms}(t)/Ma_t^2$ are shown in Figure 11. Both WENO5-AO-GKS and WENO5-AO-HLLC perform well for a wide range of Ma_t from 0.5 to 1.4. The reference data of $Ma_t = 0.5$ is obtained in [29]. When $Ma_t = 1.4$, iso-surface of the second invariant of velocity gradient tensor $Q = 25$ colored by the local Mach number at $t/\tau_0 = 1.0$ is shown in Figure 12. The results obtained by two schemes are nearly the same. The CFL number is 0.3 for both WENO5-AO-GKS and WENO5-AO-HLLC. But, WENO5-AO-GKS can take a larger CFL number 0.5 while 0.3 is the limit for WENO5-AO-HLLC in this case. When the conservative flow variables at the interface for viscous fluxes are obtained by sixth-order central difference method, the WENO5-AO-HLLC can only work for Ma_t up to 0.6, which is much smaller than 1.4. In the simulations, to improve the robustness of WENO5-AO-HLLC scheme, the conservative variables at the cell interface $Q_{i+1/2}$ are obtained by simple averaging of the left and right interface values of WENO5-AO reconstruction. The above results show that WENO5-AO-GKS is more robust than WENO5-AO-HLLC in this case.

3.3.3. Taylor-Green vortex

The three-dimensional Taylor-Green vortex is studied by WENO5-AO-GKS and WENO5-AO-HLLC. The computational domain is $[-\pi L, \pi L] \times [-\pi L, \pi L] \times [-\pi L, \pi L]$, and the initial condition is

$$U = U_0 \sin(x/L) \cos(y/L) \cos(z/L),$$

$$V = -U_0 \cos(x/L) \sin(y/L) \cos(z/L),$$

$$W = 0,$$

$$p = p_0 + \rho_0 U_0^2 (\cos(2x/L) + \cos(2y/L)) (\cos(2z/L) + 2) / 16.$$

The simulation has $L = 1$, $U_0 = 1$, $\rho_0 = 1$, and the Reynolds number $Re = U_0 L / \nu = 280$. The Mach number is $Ma = U_0 / C = 0.1$ and the sound speed is $C = \sqrt{\gamma RT}$. The mesh number is 64^3 , and periodic boundary condition is imposed at all boundaries. The volume-averaged kinetic energy is defined as,

$$E_k = \frac{1}{\rho_0 \Omega} \int_{\Omega} \frac{\rho (U^2 + V^2 + W^2)}{2} d\Omega,$$

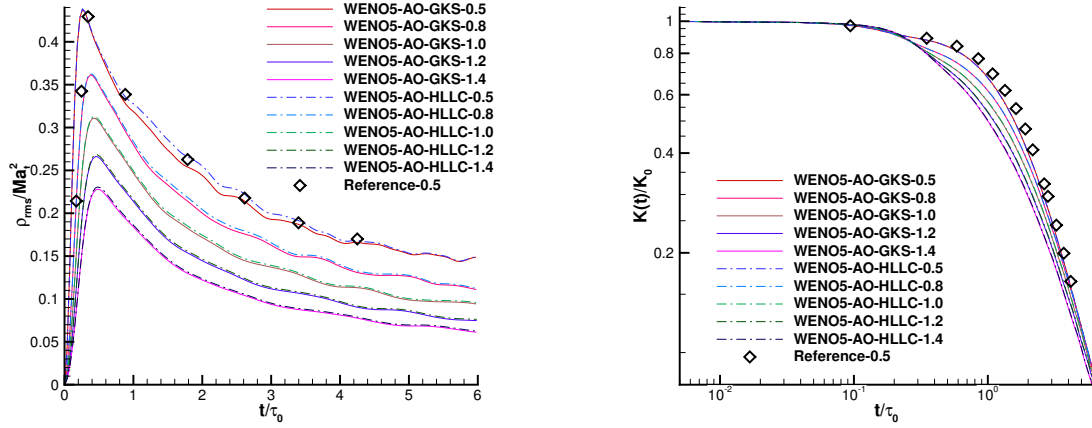


Figure 11: Compressible isotropic turbulence at different Ma_t by WENO5-AO-GKS scheme and WENO5-AO-HLLC scheme. The normalized kinetic energy (left) and normalized root-mean-square of density fluctuation (right). The CFL number is 0.3 for both WENO5-AO-GKS scheme and WENO5-AO-HLLC scheme. For all cases, the mesh number is 128^3 .

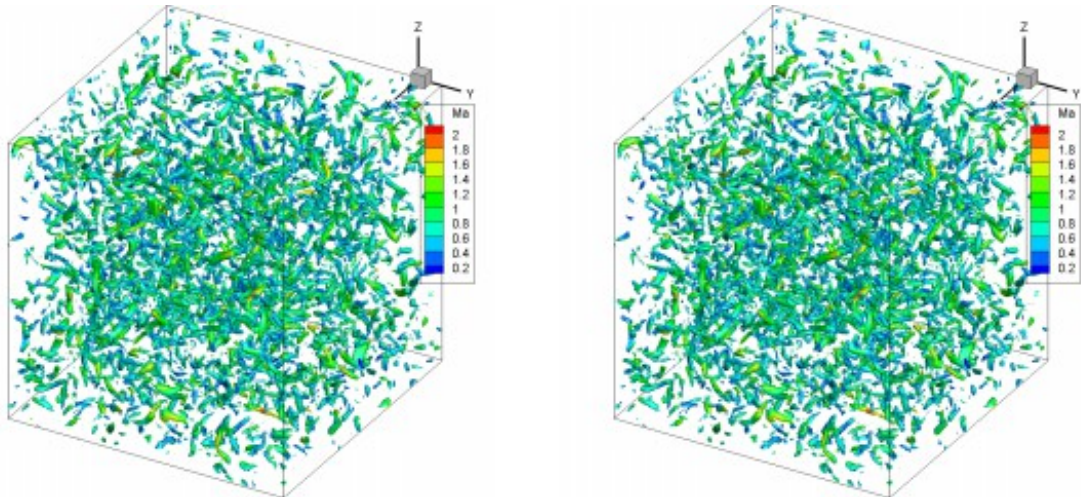


Figure 12: Compressible isotropic turbulence with $Ma_t = 1.4$: iso-surface of the second invariant of velocity gradient tensor $Q = 25$ colored with local Mach number by WENO5-AO-GKS scheme (left) and WENO5-AO-HLLC scheme (right). The mesh number is 128^3 and output time is $t/\tau_0 = 1.0$.

where Ω is the total volume of flow field. Besides, the dissipation rate of the kinetic energy is given by

$$\epsilon_k = -\frac{dE_k}{dt}.$$

The linear reconstruction is taken for both schemes in this test case. The results are presented in Figure 13, and are compared with the reference solution of [27]. The CFL number is 0.5 for WENO5-AO-GKS while 0.3 for WENO5-AO-HLLC. When CFL number is 0.4, WENO-AO-HLLC will generate large oscillation.

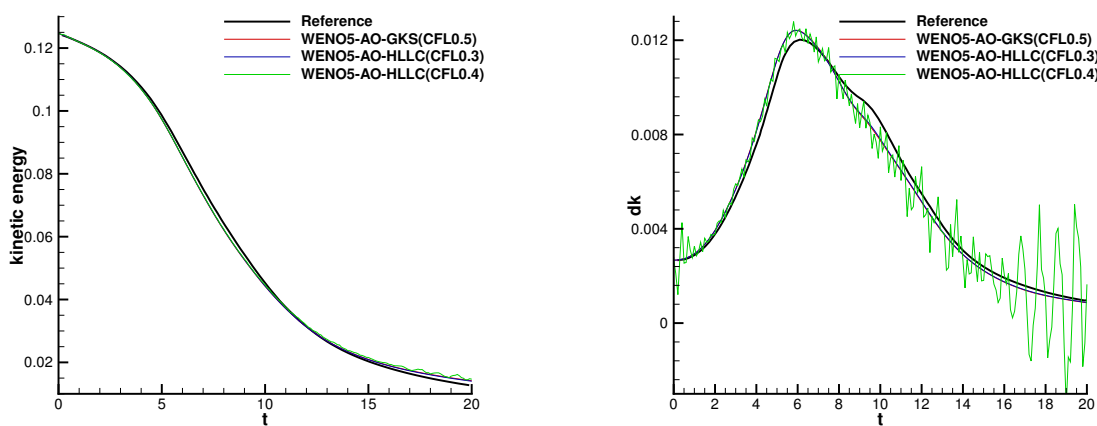


Figure 13: Taylor-Green vortex problem with $Re = 280$ by WENO5-AO-GKS scheme and WENO5-AO-HLLC scheme: the kinetic energy (left) and the dissipation rate (right). The CFL number is 0.5 for WENO5-AO-GKS scheme and 0.3 for WENO5-AO-HLLC scheme. For both cases, the mesh number is 64^3 .

4. Computational efficiency

The computational efficiency of WENO5-AO-GKS and WENO5-AO-HLLC is compared in 2-D and 3-D cases. For both schemes, the main computational cost includes two parts, reconstruction, and evolution. For the reconstruction, WENO5-AO-HLLC needs only point-wise conservative variables, while the derivatives are also needed in WENO-AO-GKS. However, additional reconstruction through central difference method for the viscous terms is required in WENO5-AO-HLLC. For the evolution stage, the GKS flux is more expensive than HLLC, but GKS uses two stages instead of four stages in HLLC to achieve 4th-order time accuracy.

The viscous shock tube is used to test the computational efficiency. The mesh points in the test are 1000×500 . The viscous flux in WENO-AO-HLLC is obtained through sixth order central difference method, where the inviscid and viscous terms are coupled in the GKS flux. The WENO5-AO reconstruction is based on characteristic variables for both schemes. In this case, the computation time and the relative efficiency are listed in Table 3. The computation times shown in Table 3 are obtained for 10 time steps by a single Intel core

i7-9700 @ 3.00GHz. The results show that WENO5-AO-HLLC is 27% more expensive than WENO5-AO-GKS in the 2-D viscous problem. The next test is the compressible isotropic turbulence in 3-D. Again, the WENO5-AO reconstruction is based on characteristic variables for both schemes. The computational time is collected by running the code for 10 time steps, and the results are shown in Table 4. The calculation time of WENO5-AO-HLLC is about 15% less than WENO5-AO-GKS. This is mainly due to the three-dimensional reconstruction, where the reconstruction in two tangential directions on both sides of a cell interface is needed in WENO-AO-GKS, instead of one tangential direction in 2D case. In this test, WENO-AO-GKS can take a CFL number 0.5, and WENO5-AO-HLLC can take a CFL number 0.3 only. As a result, WENO5-AO-GKS can have a slightly better overall efficiency in 3D case.

	CPU time (s)	Time ratio
WENO5-AO-GKS	154.91	1.00
WENO5-AO-HLLC	196.47	1.27

Table 3: 2-D computational efficiency test of viscous shock tube problem. The mesh number is 1000×500 . The shown CPU time is obtained for 10 time steps by a single Intel core i7-9700 @ 3.00GHz.

	CPU time (s)	Time ratio
WENO5-AO-GKS	476.04	1.00
WENO5-AO-HLLC	403.03	0.85

Table 4: 3-D computational efficiency test of compressible isotropic turbulence problem with $Ma_t = 0.5$ and $CFL = 0.3$. The mesh number is 128^3 . The shown CPU time is obtained for 10 time steps by a single Intel core i7-9700 @ 3.00GHz.

5. Conclusion

A comparison of performance for two high-order schemes, namely WENO5-AO-GKS and WENO5-AO-HLLC, is presented. Both schemes use the fifth-order WENO-AO reconstruction, the differences are mainly coming from the flux functions and the temporal updating schemes. In GKS, due to the time accurate flux and its time derivative the multistage and multiderivative (MSMD) is used to update the solution. The two-stage fourth-order temporal discretization achieves a 4th-order temporal accuracy. For HLLC, four stages Runge-Kutta method is used for the time accuracy. In WENO-AO-GKS, both inviscid and viscous flux terms can be evaluated from a single time-dependent gas distribution function. In WENO5-AO-HLLC, HLLC provides inviscid flux and a sixth-order central difference method is used to discretize the viscous flux. In the 3D accuracy test, both schemes can achieve the expected order of accuracy, and WENO5-AO-GKS shows a slightly smaller absolute L^1 error. In terms of the shock and contact wave capturing, both schemes perform well and have similar robustness. With the same mesh and CFL number, WENO5-AO-GKS shows better accuracy in the double shear layer test. In the Noh problem, WENO5-AO-GKS presents favorable robustness. For the compressible isotropic turbulence and three-dimensional Taylor-Green vortex problem, WENO-AO-GKS can take a large time step

with CFL number 0.5, instead of 0.3 for WENO5-AO-HLLC. For two-dimensional viscous shock tube problems, WENO5-AO-HLLC is (27%) more expensive than WENO-AO-GKS. While for the three-dimensional viscous test, WENO5-AO-HLLC is (15%) more efficient than WENO5-AO-GKS. WENO-AO-GKS requires the reconstruction of flow variables in the normal and two tangential directions on both sides of a cell interface in the 3D case. The multi-dimensional property and the coupling of inviscid and viscous fluxes in WENO5-AO-GKS have obvious advantages when the scheme is extended to the flow computation with unstructured mesh.

References

- [1] Dinshaw S Balsara, Sudip Garain, and Chi-Wang Shu. An efficient class of WENO schemes with adaptive order. *Journal of Computational Physics*, 326:780–804, 2016.
- [2] P Batten, MA Leschziner, and UC Goldberg. Average-state Jacobians and implicit methods for compressible viscous and turbulent flows. *Journal of computational physics*, 137(1):38–78, 1997.
- [3] Prabhu Lal Bhatnagar, Eugene P Gross, and Max Krook. A model for collision processes in gases I: Small amplitude processes in charged and neutral one-component systems. *Physical Review*, 94(3):511–525, 1954.
- [4] Rafael Borges, Monique Carmona, Bruno Costa, and Wai Sun Don. An improved weighted essentially non-oscillatory scheme for hyperbolic conservation laws. *Journal of Computational Physics*, 227(6):3191–3211, 2008.
- [5] David L Brown. Performance of under-resolved two-dimensional incompressible flow simulations. *Journal of Computational Physics*, 122(1):165–183, 1995.
- [6] Guiyu Cao, Liang Pan, and Kun Xu. Three dimensional high-order gas-kinetic scheme for supersonic isotropic turbulence I: criterion for direct numerical simulation. *Computers & Fluids*, 192(104273), 2019.
- [7] Guiyu Cao, Hongmin Su, Jinxiu Xu, and Kun Xu. Implicit high-order gas kinetic scheme for turbulence simulation. *Aerospace Science and Technology*, 92:958–971, 2019.
- [8] Sydney Chapman and Thomas George Cowling. *The mathematical theory of non-uniform gases: an account of the kinetic theory of viscosity, thermal conduction and diffusion in gases*. Cambridge university press, 1970.
- [9] Bing Chen, Yan Zhang, and Xu Xu. Numerical simulation of supersonic turbulent combustion flows based on flamelet model. *Journal of Propulsion Technology*, 12:11, 2013.
- [10] Virginie Daru and Christian Tenaud. Evaluation of TVD high resolution schemes for unsteady viscous shocked flows. *Computers & Fluids*, 30(1):89–113, 2000.
- [11] SK Godunov. A finite difference method for the computation of discontinuous solutions of the equations of fluid dynamics. *Sbornik: Mathematics*, 47(8-9):357–393, 1959.
- [12] Ami Harten, Peter D Lax, and Bram van Leer. On upstream differencing and godunov-type schemes for hyperbolic conservation laws. *SIAM review*, 25(1):35–61, 1983.
- [13] Ami Harten, Stanley Osher, Björn Engquist, and Sukumar R Chakravarthy. Some results on uniformly high-order accurate essentially nonoscillatory schemes. *Applied Numerical Mathematics*, 2(3-5):347–377, 1986.
- [14] Xing Ji, Liang Pan, Wei Shyy, and Kun Xu. A compact fourth-order gas-kinetic scheme for the Euler and Navier-Stokes equations. *Journal of Computational Physics*, 372:446 – 472, 2018.
- [15] Xing Ji and Kun Xu. Performance enhancement for high-order gas-kinetic scheme based on weno-adaptive-order reconstruction. *Commun. Comput. Phys.*, 28:539–590, 2020.
- [16] Xing Ji, Fengxiang Zhao, Wei Shyy, and Kun Xu. A family of high-order gas-kinetic schemes and its comparison with Riemann solver based high-order methods. *Journal of Computational Physics*, 356:150–173, 2018.

- [17] Xing Ji, Fengxiang Zhao, Wei Shyy, and Kun Xu. A HWENO Reconstruction Based High-order Compact Gas-kinetic Scheme on Unstructured Mesh. *Journal of Computational Physics*, 109367, 2020.
- [18] Guang-Shan Jiang and Chi-Wang Shu. Efficient implementation of weighted ENO schemes. *Journal of computational physics*, 126(1):202–228, 1996.
- [19] Doron Levy, Gabriella Puppo, and Giovanni Russo. Central WENO schemes for hyperbolic systems of conservation laws. *ESAIM: Mathematical Modelling and Numerical Analysis*, 33(3):547–571, 1999.
- [20] Jiequan Li and Zhifang Du. A two-stage fourth order time-accurate discretization for Lax–Wendroff type flow solvers I. hyperbolic conservation laws. *SIAM Journal on Scientific Computing*, 38(5):A3046–A3069, 2016.
- [21] Qibing Li, Song Fu, and Kun Xu. Application of gas-kinetic scheme with kinetic boundary conditions in hypersonic flow. *AIAA journal*, 43(10):2170–2176, 2005.
- [22] Wei Liao, Yan Peng, and Li-Shi Luo. Gas-kinetic schemes for direct numerical simulations of compressible homogeneous turbulence. *Physical Review E*, 80(4):046702, 2009.
- [23] Xu-Dong Liu, Stanley Osher, Tony Chan, et al. Weighted essentially non-oscillatory schemes. *Journal of computational physics*, 115(1):200–212, 1994.
- [24] Jun Luo and Kun Xu. A high-order multidimensional gas-kinetic scheme for hydrodynamic equations. *Sci. China, Technol. Sci.*, 56(10):2370–2384, 2013.
- [25] William F Noh. Errors for calculations of strong shocks using an artificial viscosity and an artificial heat flux. *Journal of Computational Physics*, 72(1):78–120, 1987.
- [26] Liang Pan, Junxia Cheng, Shuanghu Wang, and Kun Xu. A two-stage fourth-order gas-kinetic scheme for compressible multicomponent flows. *Communications in Computational Physics*, 22(4):1123–1149, 2017.
- [27] Liang Pan and Kun Xu. Two-stage fourth-order gas-kinetic scheme for three-dimensional Euler and Navier-Stokes solutions. *International Journal of Computational Fluid Dynamics*, 32(10):395–411, 2018.
- [28] Liang Pan, Kun Xu, Qibing Li, and Jiequan Li. An efficient and accurate two-stage fourth-order gas-kinetic scheme for the Euler and Navier–Stokes equations. *Journal of Computational Physics*, 326:197–221, 2016.
- [29] Ravi Samtaney, Dale I Pullin, and Branko Kosović. Direct numerical simulation of decaying compressible turbulence and shocklet statistics. *Physics of Fluids*, 13(5):1415–1430, 2001.
- [30] Shuang Tan, Qibing Li, Zhixiang Xiao, and Song Fu. Gas kinetic scheme for turbulence simulation. *Aerospace Science and Technology*, 78:214–227, 2018.
- [31] Huazhong Tang and Tiegang Liu. A note on the conservative schemes for the Euler equations. *Journal of Computational Physics*, 218:451–459, 2006.
- [32] Vladimir A Titarev and Eleuterio F Toro. Finite-volume WENO schemes for three-dimensional conservation laws. *Journal of Computational Physics*, 201(1):238–260, 2004.
- [33] SA Tokareva and Eleuterio F Toro. HLLC-type Riemann solver for the Baer–Nunziato equations of compressible two-phase flow. *Journal of Computational Physics*, 229(10):3573–3604, 2010.
- [34] Eleuterio F Toro. *Riemann solvers and numerical methods for fluid dynamics: a practical introduction*. Springer Science & Business Media, 2013.
- [35] Eleuterio F Toro. The HLLC Riemann solver. *Shock Waves*, 29:1065–1082, 2019.
- [36] Eleuterio F Toro, Michael Spruce, and William Speares. Restoration of the contact surface in the HLL-Riemann solver. *Shock waves*, 4(1):25–34, 1994.
- [37] Paul Woodward and Phillip Colella. The numerical simulation of two-dimensional fluid flow with strong shocks. *Journal of computational physics*, 54(1):115–173, 1984.
- [38] Kun Xu. BGK-based scheme for multicomponent flow calculations. *Journal of Computational Physics*, 134(1):122–133, 1997.
- [39] Kun Xu. Gas-kinetic schemes for unsteady compressible flow simulations. *Lecture series-van Karemman Institute for fluid dynamics*, 3:C1–C202, 1998.
- [40] Kun Xu. A gas-kinetic BGK scheme for the Navier–Stokes equations and its connection with artificial dissipation and Godunov method. *Journal of Computational Physics*, 171(1):289–335, 2001.
- [41] Kun Xu and Juan-Chen Huang. A unified gas-kinetic scheme for continuum and rarefied flows. *Journal*

- of Computational Physics*, 229(20):7747–7764, 2010.
- [42] Rui Zhang, Mengping Zhang, and Chi-Wang Shu. On the order of accuracy and numerical performance of two classes of finite volume WENO schemes. *Communications in Computational Physics*, 9(3):807–827, 2011.
 - [43] Fengxiang Zhao, Xing Ji, Wei Shyy, and Kun Xu. An acoustic and shock wave capturing compact high-order gas-kinetic scheme with spectral-like resolution. *arXiv preprint arXiv:2001.01570*, 2019.
 - [44] Fengxiang Zhao, Xing Ji, Wei Shyy, and Kun Xu. Compact higher-order gas-kinetic schemes with spectral-like resolution for compressible flow simulations. *Advances in Aerodynamics*, 1(1):13, 2019.
 - [45] Jun Zhu and Chi-Wang Shu. A new type of multi-resolution WENO schemes with increasingly higher order of accuracy. *Journal of Computational Physics*, 375:659–683, 2018.